The International Journal of Advanced Manufacturing Technology (2022) 118:3209–3227
https://doi.org/10.1007/s00170-021-08080-5

ORIGINAL ARTICLE

Analytical modelling of cutting forces in ultra-precision fly grooving considering effects of trans-scale chip thickness variation and material microstructure

Zhanwen Sun[1,2] · Suet To[2] · Peizheng Li[1] · Sujuan Wang[1] · Tao Zhang[1]

Received: 13 May 2021 / Accepted: 15 September 2021 / Published online: 12 October 2021

Abstract

Although ultra-precision fly grooving (UPFG) is widely applied to fabricate micro-structured surfaces, few studies have focused on the cutting force model of UPFG. The unique kinematics of UPFG leads to the trans-scale variation of undeformed chip thickness from nanoscale to microscale, in which case the influence of material microstructure and size effect is prominent. This study proposes an analytical cutting force model for UPFG with full consideration of the kinematics, chip formation mechanism, material microstructure, material elastic recovery, size effect, and tool geometry. Specifically, by correlating micro-forming theory to crystal plastic theory, a hybrid slip-line model (HSLM) is developed to determine the flow stress in primary deformation zone, which can quantify the influence of size effect and microstructure, such as grain size, grain boundary, dislocation density, and crystal anisotropy, on flow stress. Then, the normal cutting force and frictional cutting force are estimated by analyzing the stress distribution and frictional states at tool-chip interface. The rubbing force induced by material elastic recovery is determined based on indentation theory. Finally, the models are experimentally validated by fly cutting of polycrystalline copper with different machining parameters, and it is also demonstrated that the proposed HSLM can capture the periodic transformation of cutting mechanism in UPFG from ploughing (compressive stress) to shearing (tensile stress) with tool rotation.

Keywords Ultra-precision fly grooving · Analytical cutting force model · Micro/nano-cutting mechanism · Material microstructure

Nomenclature

o_s-$x_s y_s z_s$	Coordinate system built on spindle
o_w-$x_w y_w z_w$	Coordinate system built on workpiece
o_t-$x_t y_t z_t$	Coordinate system built on tool center point
f_e	Feed rate of UPFG
d_0	Depth of cut
$\varphi_{i,j}$	The j-th discrete angle at the i-th rotational angle
w_i	Width for the discrete element at i-th chip cross-section
S_v	Spindle rotational speed
$\sigma_s \sigma_i$	Flow stress of surface grains and inner grains
η	Size factor
τ_R	Critical resolved shear stress
D	Grain size
α_d	Constant describing dislocation interaction
b_v	Burger vector
$k_R\, n$	Coefficients related to critical resolved shear stress
C_1	Material related constant
$T_w\, T_m\, T_0$	Working temperature, melting temperature and room temperature
$\phi_{i,j}$	Shear angle
$v_{sh}^{i,j}$	Velocity along shear band
v	Cutting speed
ζ	Coefficient related to equivalent tool-chip contact length
r_e	Tool edge radius
$a\, b$	Coefficients related to shear angle
ρ	Density of the workpiece

✉ Sujuan Wang
grace.wangsj@gdut.edu.cn

[1] State Key Laboratory of Precision Electronic Manufacturing Technology and Equipment, School of Electromechanical Engineering, Guangdong University of Technology, Guangzhou, China

[2] State Key Laboratory in Ultra-Precision Machining Technology, Department of Industrial and Systems Engineering, The Hong Kong Polytechnic University, Kowloon, Hong Kong, China

$\beta^{'}$	Heat dissipation coefficient
$\sigma_A^{i,j}\ \sigma_B^{i,j}$	Hydrostatic flow stress at point A and B
s	Distance along equivalent tool rake face
$l_c^{i,j}$	Tool-chip contact length
r	Coefficient related to tool-chip contact length
l_s^i	Length of the chip sticking region
$F_n^{i,j}\ F_f^{i,j}$	Nominal cutting force and frictional cutting force
$\psi_{i,j}$	Inclination angle between the equivalent rake face and z-axis
d_c	Critical depth of cut
k_r	Rubbing force coefficient
$F_{c,r}^{i,j}\ F_{t,r}^{i,j}$	Rubbing force in cutting and thrust direction
$\zeta^{'}$	Damping ratio of dynameter
ω_n	Oscillation frequency without damping
S_w	Swing radius of diamond tool
ϑ	Damping angle
$\Delta\theta$	Discrete angle of the rotational tool
$\Delta\varphi$	Discrete angle of the chip cross-section
R_t	Tool nose radius
θ_i	The i-th rotational angle
$t_c^{i,j}$	Undeformed chip thickness of the discrete element
$N_s\ N_i\ N_t$	Grain numbers of surface layer, inner layer and whole workpiece
t_i	Discrete time
$M\ m$	Orientation factors for polycrystal and single crystal
$\sigma\ \varepsilon\ \dot{\varepsilon}$	Stress, strain and strain rate
k	Grain boundary related stress
μ_p	Shear module for different phases
τ_R	Critical resolved shear stress for single crystal
ρ_T	Total dislocation density
$A\ B\ C\ p\ q$	Parameters of Johnson–Cook equation
$\gamma_e^{i,j}$	Equivalent tool rake angle
$\tau_s\ \gamma_s\ \dot{\gamma}_s$	Equivalent flow stress, strain and strain rate
C_0	Coefficient related to strain rate
$l_{AB}^{i,j}$	Length of shear band
γ_0	Tool rake angle
$s_1\ s_2$	Distance parallel and vertical to the shear band
$D^{'}$	Size effect coefficient
β	Friction angle
S_T	Specific heat in cutting region
$v_\perp$	Velocity vertical to shear band
ς	Angle between the resultant force and shear band
ξ	Coefficient characterize the pressure distribution
$\sigma_n^{i,j}\ \sigma_f^{i,j}$	Normal stress and frictional stress
μ_f	Friction coefficient on tool rake face
κ	Tool clearance angle
$F_{c,s}^{i,j}\ F_{t,s}^{i,j}$	Cutting force and thrust force for the i-th discrete element
$\Lambda_{i,j}$	Tool-workpiece interference volume
μ_r	Friction coefficient of rubbing
$F_c^{i,j}\ F_t^{i,j}$	Total cutting and thrust force
$F_x^{i,j}\ F_z^{i,j}$	Total cutting force in x-axis and z-axis direction
ω_d	Oscillation frequency

1 Introduction

Ultra-precision fly grooving (UPFG) is widely regarded as a promising technology to fabricate micro/nano-structured functional surfaces, due to its ability to achieve submicron form accuracy and nanometric surface roughness [1, 2]. To promote the widespread application of UPFG, it is of great importance to investigate the efficient modelling methods of the cutting forces, as the prediction of cutting force is the premise of optimizing cutting parameters [3], understanding the tool-workpiece interactions [4] and monitoring tool wear [5]. Besides, cutting force model is the basis for some innovative machining technologies, such as forced-controlled servo cutting, in which cutting force serves as the feedback signal of the tool servo motion to improve the machining accuracy of freeform surfaces. For example, Chen et al. [6] proposed a cutting force auto-tracking method to fabricate micro-structured surfaces on brittle materials, which can highly improve the form accuracy and flexibility compared with conventional methods.

In UPFG, the diamond tool rotates with a large swing radius, so the diamond tool intermittently contacts and departs the workpiece. The unique kinematics of UPFG results in very thin chip morphology [7]. Besides, the shape of tool-workpiece engagement area in UPFG constantly changes with tool rotation, and the average undeformed chip thickness (UDCT) periodically changes between a few nanometers and a few micrometers for each tool rotational cycle [8]. At this cutting scale, the diamond tool cuts a few grains or even a single grain of the workpiece material. Thus, the material microstructure, such as grain size, grain boundary, dislocation density, and crystal anisotropy, has a strong impact on the cutting mechanism and the micro-mechanics properties of the workpiece material in cutting region [9]. Besides, due to the trans-scale variation of UDCT ranging between nanoscale and microscale in UPFG, the influence of size effect on cutting force cannot be neglected either [10]. Besides, it is worth to note that the intermittent cutting process of UPFG also results in the coupling phenomenon between the cutting force signal and the free-vibration signal of the dynameter, so the previously proposed force models for ball end milling or turning processes cannot be used to

estimate cutting force for UPFG. Even though researchers have been proposed many studies on the surface generation, tool wear, and machining error analysis for UPFG, few studies have focused on theoretical modeling of the cutting forces of UPFG. The correlation of material microstructure on the determination of flow stress is necessary to improve the estimation accuracy of cutting force model for UPFG.

According to the employed modelling theory, the current cutting force models basically consist in three types, namely, empirical model, numerical model, and analytical model. For example, Huang et al. [11] proposed an empirical cutting force model for diamond turning by considering tool edge radius effect and material elastic recovery. Without fully understanding the internal cutting mechanism, empirical models generally require a large number of experiments to determine the force coefficients, which is low efficient and has relatively weak applicability in other cutting conditions. In contrast, analytical models derived by deeply analyzing the tool-workpiece interactions are more scientific and practical and have drawn an increasing attention by researchers. Zhu et al. [4] investigated the dynamic cutting forces generated in slow tool servo turning using both analytical and finite element modelling methods. An analytical force model in diamond sculpturing of micro-structured surfaces was proposed by Sun et al. [12] though deeply investigating the influence of cutting direction on material removal. Fernando et al. [13] developed a mechanistic model for rotary ultrasonic machining of rock considering both ductile and brittle material removal mechanism. Zhu et al. [14] employs screw theory to describe the cutter spatial motion, based on which the analytical cutting force model is proposed for milling processes. Current analytical models have developed by thoroughly incorporating dynamics, plastic mechanics, thermal physics, and friction actions, thereby achieving relatively high estimation accuracy of cutting forces for both turning and milling processes. However, these models are still unreliable to predict the cutting force for UPFG featuring unique kinematics and a trans-scale variation of UDCT from microscale to nanoscale.

With the significant scaling down of the UDCT in ultra-precision machining, size effect that relates to the special micro-mechanics of the workpiece material becomes increasingly prominent in terms of material removal mechanism. Gap-Yong et al. [15] and Ran et al. [16] stated that size effect majorly results from the remarkable reduction of the grain numbers in the deformation zone, in which case individual grains become crucial and the macroscope mechanics principles may be inapplicable. Chen et al. [17] experimentally studied the size effect in micro-milling and found that the surface roughness highly increases when the ratio of feed rate to tool edge radius is lower than a critical value. By applying nanoindentation on different metal alloys, Kim et al. [18] found that the hardness of metal alloys greatly increases with the decrease of indentation size, named as indentation size effect. To provide a theoretical explanation on size effect, a surface layer model was proposed by Lai et al. [19]. The uniqueness of this model is the incorporation of a size factor into the Armstrong's model to describe the different mechanics properties between the surface layer and inner layer. They suggested that the reduction of the flow stress with the minimization of specimen is attributed to the less restriction of the dislocation sliding in the surface layer grains. Overall, it is learned that size effect plays a key role in UPFG and other ultra-precision machining technologies.

In analytical modelling of cutting force, slip-line theory is generally used to analyze the chip formation and material removal process in cutting zone. Currently, slip-line models have developed from macroscope to microscope by considering equivalent negative rake angle as well as by ever-refining the shear band. Fang et al. [20] proposed a slip-line model featuring curved shear band to account for the curled chip formation mechanism and the chip back-flow behavior in cutting process. Ke et al. [21] theoretically demonstrated the saw-tooth chip formation mechanism by in-depth investigating the shear-slip geometry of the slip-line field. To model the extrusion force in micro-cutting, Ren et al. [22] reported an extend slip-line model that detailly describes the flow direction of the trapped metal beneath the cutting edge. Recently, Cheng et al. [23] proposed a modified slip-line model by considering the equivalent negative rake angle, tool-chip friction, and thermal distribution in micro-cutting process. Nevertheless, the current slip-line models generally overlook the impact of microstructure and size effect on the material deformation.

UPFG features unique chip formation mechanism, and the influence of material microstructure and size effect is prominent in UPFG, resulting in the difficulties on efficiently estimate the cutting forces. Facing this dilemma, an analytical cutting force model of UPFG is proposed in this study with the full consideration of the kinematics, chip formation, material microstructure, size effect, material elastic recovery, and tool geometry. The chip formation mechanism of UPFG is firstly studied to mathematically describe the chip morphology. In consideration of the trans-scale variation of UDCT, a hybrid slip-line model (HSLM) is developed to quantitatively present the influence of material microstructure and size effect on the flow stress. Then, the cutting forces are determined based on the distribution of the normal stress and frictional stress at tool-chip interface. Besides, the rubbing force induced by the material elastic recovery is determined based on indentation theory. The free-vibration force generated by the vibration of dynamometer is also determined by proposing a two-order dynamic model. The proposed models are experimentally validated by measuring the cutting forces in UPFG and observing the chip morphologies.

2 Analytical cutting force model of UPFG

In UPFG, the tool-workpiece contact duration of each tool rotational cycle is very short, so the collected cutting force signals is similar to a serious of impulse signals, as shown in Fig. 1a. An enlarged view of the cutting force signals for one tool rotational cycle is shown in Fig. 1b. It is observed that the cutting force signal is coupled by two parts. One is the impulse cutting force generated by tool-workpiece interaction, and the other one is the free-vibration force of the force sensor induced by the force impulse. It is worth to note that the force sensor is component by a serious of force sensitive element, i.e., piezoelectric ceramics, whose mechanical property can be approximately regarded as a second-order dynamic system, as illustrated in Fig. 1c. In this section, the kinematics and chip formation mechanism of UPFG are firstly introduced to mathematically describe the chip morphology, and then the modelling processes of impulse cutting force and free-vibration force are introduced.

2.1 Kinematics and chip formation mechanism of UPFG

The kinematics of UPFG and chip formation mechanism are schematically illustrated in Fig. 2. A diamond tool is clamped on the rotational spindle with a large swing radius, while the workpiece is fixed on the linear guide. Different from ball end milling, the rotational axis of the spindle is parallel to the workpiece surface in UPFG. Thus, most proportion of each tool rotational cycle is idling, and the real cutting duration is very short. Through the feed motion of the rotational diamond tool along feed direction, micro-grooves can be fabricated on the workpiece surface, as illustrated by the blue lines in Fig. 2a. After finishing the fabrication of one groove, the diamond tool moves back to the origin point with a step distance in raster direction (y_s-axis direction) to fabricate the next groove. The unique intermittent cutting process of UPFG results in the axisymmetric chip morphology, as shown in Fig. 2 b and c. According to the kinematics of UPFG, each piece of the chip is generated by two successive cutting processes, and each chip is composed of three surfaces, namely, the top surface formed by previous rotary cutting, bottom surface formed by current rotary cutting, and the original surface of the workpiece. To mathematically describe the chip morphology, a coordinate system o_s-$x_s y_s z_s$ is built on the spindle with the z_s-axis vertical to the workpiece surface. The three surfaces of the chip can be mathematically expressed by

$$\begin{cases} \left(\sqrt{x^2+z^2}-S_w+R_t\right)^2+y^2=R_t^2 \\ \left(\sqrt{\left(x+f_e\right)^2+z^2}-S_w+R_t\right)^2+y^2=R_t^2 \\ z=S_w-d_0 \end{cases} \tag{1}$$

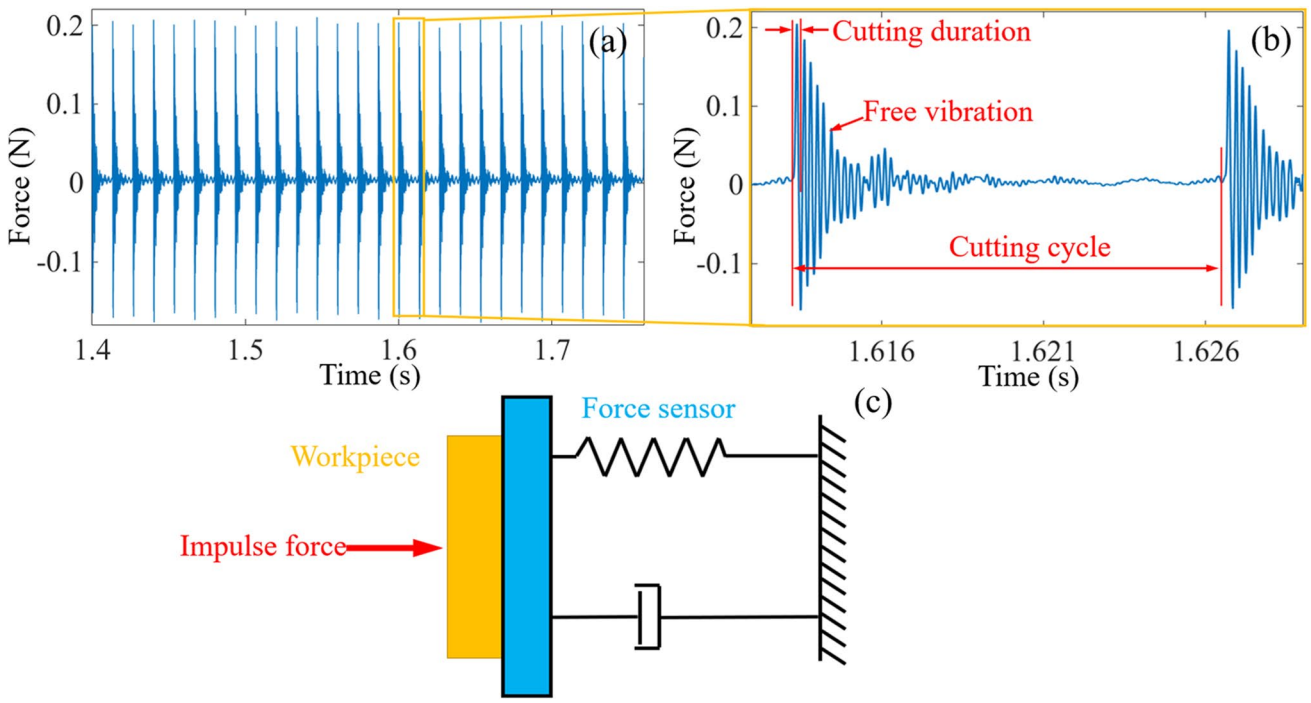

Fig. 1. **a** Measured cutting force signal in UPFG and **b** an enlarged view of one rotational cycle, **c** schematic of the generation of free-vibration force in UPFG.

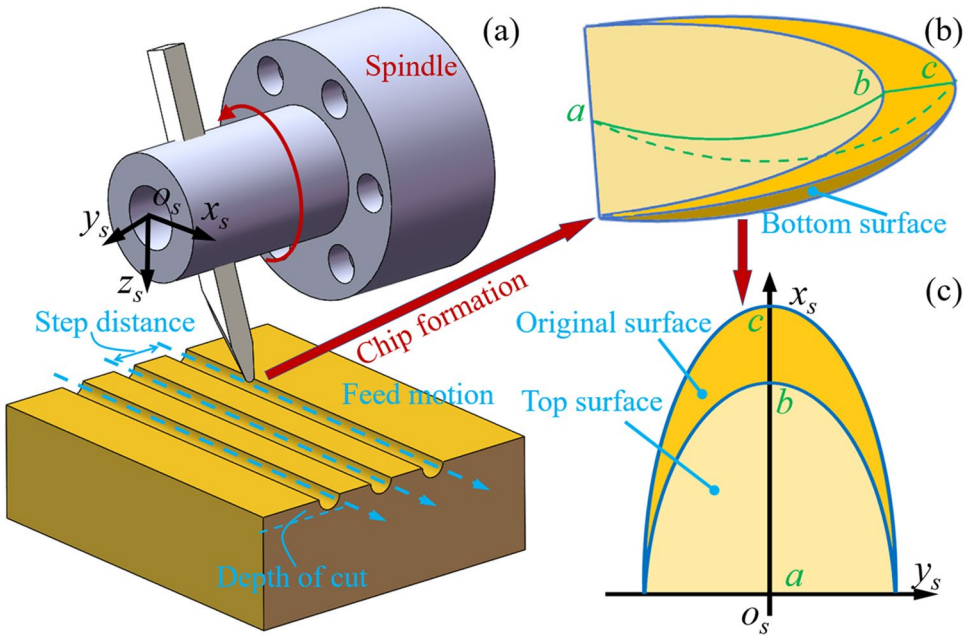

Fig. 2 Schematic of the **a** kinematics of UPFG, the **b** three-dimensional chip morphology, and **c** two-dimensional chip morphology

where S_w and S_r are the swing radius of diamond tool and the step distance in raster direction, d_0 denotes the depth of cut (DoC), R_t is the tool nose radius, and f_e is the feed rate.

The chip formation process of UPFG from the view of y_s-axis direction is shown in Fig. 3a. The diamond tool initially contacts the workpiece at point a and then departs at point c. The corresponding rotational angles for points a, b, and c can be expressed as

$$\begin{cases} \theta_a = -\arcsin\left(\frac{f_e}{2S_w}\right) \\ \theta_b = \arctan\left(\frac{x_b}{z_b}\right) \\ \theta_c = \arctan\left(\frac{x_c}{z_c}\right) \end{cases} \tag{2}$$

where x_b, z_b, x_c, and z_c are the coordinates of the points b and c, respectively, which can be determined by simultaneously solving expressions in Eq. (1). As the cross-sectional area of the chip changes with tool rotation, the rotational angle of each cutting cycle is evenly discretized by a specific angle ($\Delta\theta$) to accurately calculate the instantaneous chip thickness. When the i-th rotational angle (θ_i) is intermediate between θ_a and θ_b (case 1), the cross-sectional profile of the chip is shown in Fig. 3b, or otherwise (case 2) the cross-sectional profile changes to the shape shown in Fig. 3c. To mathematically describe the change of the chip thickness along y_s-axis direction, another coordinate system o_t-$y_t z_t$ is built on the cutter location point (CLP) with the y_t-axis parallel to y_s-axis direction. The i-th cross-sectional profile is further discretized by a specific angle ($\Delta\varphi$). According to the geometrical relation, for case 1, the chip thickness ($t_c^{i,j}$) at the i-th rotational angle (θ_i) and j-th discrete angle ($\varphi_{i,j}$) is the straight line distance from the curves l, m, or n to curve h, as shown in Fig. 3b. The coordinates of the points ($x_0^{i,j}$,$y_0^{i,j}$,$z_0^{i,j}$) on curves l, m, and n can be uniformly expressed by

$$x_0^{i,j} = z_0^{i,j} tan\theta_i \tag{3}$$

$$y_0^{i,j} = tan\left(\varphi_{i,j}\right)\left[z_0^{i,j} - \left(S_w - R_t\right)cos\theta_i\right] \tag{4}$$

$$\begin{cases} z_0^{i,j} = S_w - d_0 & \varphi_A^i \ll \varphi_{i,j} < \varphi_B^i or \varphi_C^i \ll \varphi_{i,j} \ll \varphi_D^i \\ z_0^{i,j} = \sqrt{\left(\sqrt{R_t^2 - y_0^{i,j^2}} - S_w + R_t\right)^2 - \left(x_0^{i,j} + f_e\right)^2} & \varphi_B^i \ll \varphi_{i,j} < \varphi_C^i \end{cases} \tag{5}$$

where the angles φ_A^i, φ_B^i, φ_C^i, and φ_D^i can be determined by combining Eq. (3), Eq. (4), and Eq. (1). Similarly, for case 2, the coordinates of the points ($x_0^{i,j}$,$y_0^{i,j}$,$z_0^{i,j}$) on curves l can be by substituting Eq. (3) and Eq. (4) into the following expression:

$$z_0^{i,j} = S_w - d_0 \tag{6}$$

As shown in Fig. 3 b and c, the coordinates of the points ($x_1^{i,j}$,$y_1^{i,j}$,$z_1^{i,j}$) on curves h can be expressed by

$$\begin{cases} x_1^{i,j} = z_1^{i,j}\tan\theta_i \\ y_1^{i,j} = \tan\left(\varphi_{i,j}\right)\left[z_1^{i,j} - \left(S_w - R_t\right)\cos\theta_i\right] \\ z_1^{i,j} = \sqrt{\left(\sqrt{R_t^2 - y_0^{i,j^2}} - S_w + R_t\right)^2 - \left(x_0^{i,j} + f_e\right)^2} \end{cases} \tag{7}$$

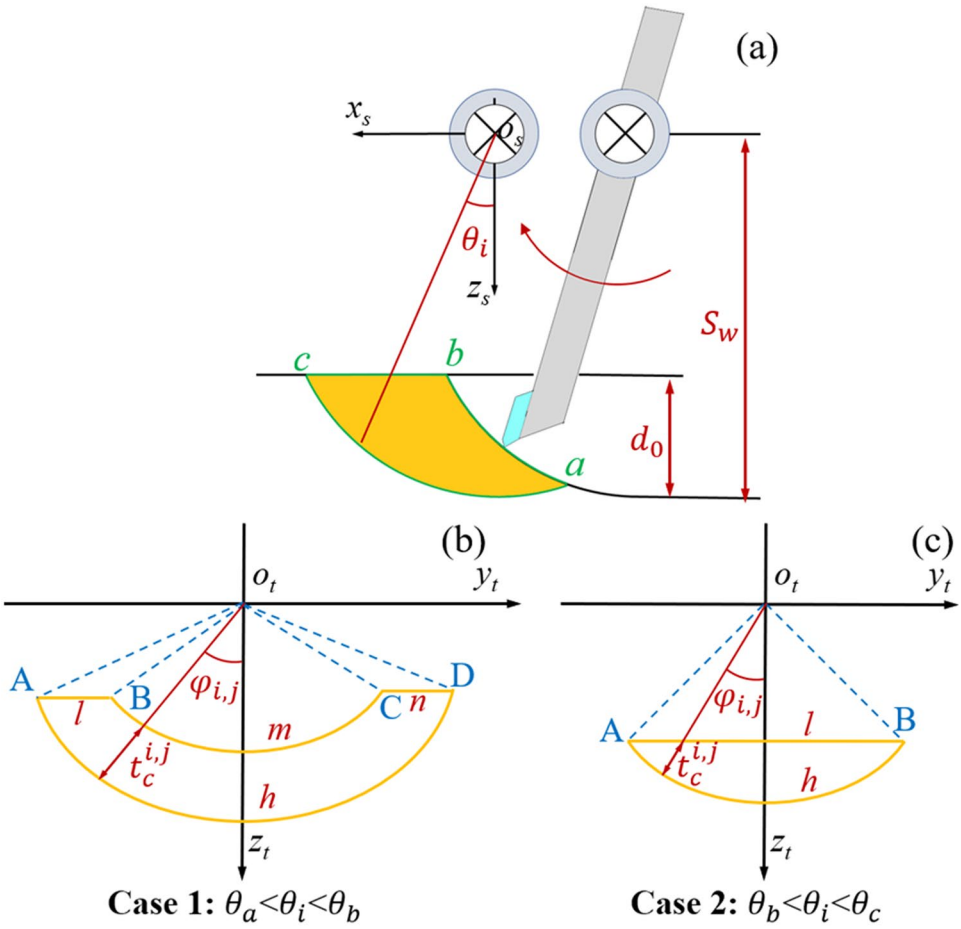

Fig. 3 Schematic of the **a** chip formation of UPFG from the view in y_s-axis direction, **b**,**c** the cross-sectional profiles of the chip for case 1 and case 2

Accordingly, the instantaneous UDCT ($t_c^{i,j}$) at the i-th rotational angle (θ_i) and j-th discrete angle ($\varphi_{i,j}$) can be calculated by

$$t_c^{i,j} = \sqrt{\left(x_1^{i,j} - x_0^{i,j}\right)^2 + \left(y_1^{i,j} - y_0^{i,j}\right)^2 + \left(z_1^{i,j} - z_0^{i,j}\right)^2} \tag{8}$$

In this study, each discrete element is treated as an independent process; the corresponding width (w_i) and time (t_i) can be expressed by

$$w_i = \Delta\varphi R_t \tag{9}$$

$$t_i = \frac{60\theta_i}{2\pi S_v} \tag{10}$$

where S_v denotes the spindle rotational speed of UPFG.

2.2 Trans-scale cutting force model

For the discrete orthogonal cutting elements having UDCT larger than the critical uncut chip thickness, normal cutting force and frictional cutting force are generated at the tool-chip interface due to the material plastic deformation. By combining crystal plastic theory and slip-line theory, the cutting force for orthogonal cutting is modeled in this section with the consideration of size effect, microstructure, tool-chip contact states, tool geometry, and temperature.

2.2.1 Calculation of flow stress by hybrid slip-line model

It is known from metal sheet micro-forming theory that the ratio of grain size to sheet thickness has a strong correlation with the material micro-mechanics properties during micro-plastic deformation [24, 25]. Similarly, in the scenario of ultra-precision diamond cutting, size factor (SF) defined as the ratio of the grain size to UDCT greatly influences flow stress when the cutting scale drops from millimeters to micrometers or even nanometers. To accurately calculate the size factor-dependent flow stress, a hybrid slip-line model (HSLM) describing UPFG of polycrystalline metals is proposed on the basis of Oxley's model by fully considering the material microstructure and size effect, as shown Fig. 4. A coordinate system *ow-xwywzw* is fixed on the workpiece with *xw*-axis in accordance with the cutting direction. The feature of the proposed hybrid model is the division of the workpiece

into two layers according to the UDCT, namely, surface layer (shaded by yellow) and inner layer (shaded by pink). In the micro/nano-cutting process, the surface layer grains are compressed by the tool rake face, resulting in the plastic deformation of the workpiece material along shear band as well as the formation of the chip at the tool-chip interface.

According to the "surface layer model" of micro-forming process, the grains located in the cutting region is less restricted than the ones inside the workpiece [19]. Besides, the share of the surface grains increases with the increase of size factor, so the flow stress (σ) of the deformed material can be formulated by

$$\sigma = \frac{N_s\sigma_s + N_i\sigma_i}{N_t} = \eta\sigma_s + (1-\eta)\sigma_i \tag{11}$$

where N_s and N_i represent the number of the grains in the surface layer and inner layer; N_t is the total grain number. σ_s and σ_i denote the flow stress of surface grains and inner grains, respectively, and η is size factor. According to the famous Hall–Petch equation, the mechanics properties of the surface layer grains is similar to single crystal, while that of inner layer grains similar to polycrystal. Therefore, the flow stress of the surface layer grains and inner layer grains can be expressed by

$$\sigma_s = m\tau_R(\varepsilon) \tag{12}$$

$$\sigma_i = M\tau_R(\varepsilon) + \frac{k}{\sqrt{D}} = M\tau_R(\varepsilon) + \alpha_d\mu_p b_v\sqrt{\rho_T} \tag{13}$$

where m and M are the orientation factors that represent the effect of crystal anisotropy for single crystal and polycrystal, respectively.k represents the necessary stress required to propagate general yield across the polycrystal grain boundaries, which is determined by the dislocation density. D is the grain size. α_d is the constant describing the dislocation interaction, μ_p is the shear module for different phases, b_v is the Burger vector, and ρ_T is the total dislocation density. Thereby, the second term of Eq. (13) corelates the material microstructure factors to flow stress. $\tau_R(\varepsilon)$ denotes the critical resolved shear stress for single crystal, which can be expressed as an exponential function of strain $k_R\varepsilon^n$ according to crystal plastic theory. Ashby et al. [26] classifies the total dislocations into two types, namely, statistically stored dislocation and geometrically necessary dislocation. When the gain size is similar in the cutting zone, the influence of statistically stored dislocation can be neglected [16], and ρ_T can be expressed by

$$\rho_T = \frac{C_1\varepsilon}{b_v D} \tag{14}$$

where C_1 is the material related constant. Hence, the quasi-static flow stress of deformed material in micro/nano-cutting can be expressed by combining the size dependent and size independent parts as

$$\sigma(\varepsilon) = \left(Mk_R\varepsilon^n + \alpha_d\mu_p b_v\sqrt{\frac{C_1\varepsilon}{b_v D}}\right) - \eta\left(Mk_R\varepsilon^n + \alpha_d\mu_p b_v\sqrt{\frac{C_1\varepsilon}{b_v D}} - mk_R\varepsilon^n\right) \tag{15}$$

It is worth to note that Eq. (15) describes the stress–strain relation of polycrystalline metals under quasi-static deformation. With the consideration of the strain rate and thermal effect, the constitutive relation of workpiece material can be described by the well-known Johnson–Cook equation, in which the flow stress is formulated as a product of three terms representing the effect of strain, strain rate, and working temperature, respectively, as the following equation:

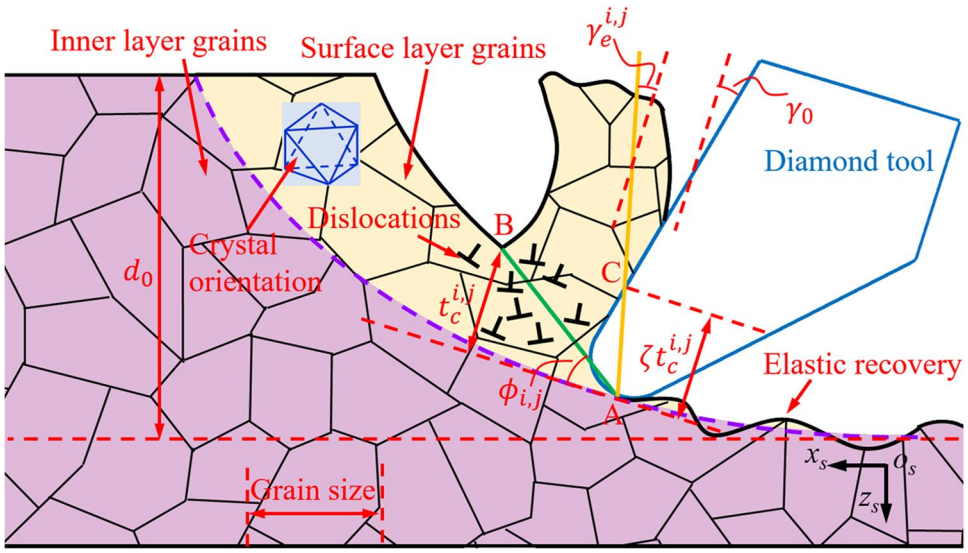

Fig. 4 Schematic of the hybrid slip-line model considering material microstructures and size effect

$$\sigma(\varepsilon) = \left[A + B\varepsilon^{p}\right]\left[1 + Cln\left(\frac{\dot{\varepsilon}}{\varepsilon_0}\right)\right]\left[1 - \left(\frac{T_w - T_0}{T_m - T_0}\right)^{q}\right] \quad (16)$$

The first term of Johnson–Cook equation is designed as $A + B\varepsilon^{p}$ to make the stress–strain curve fitting easier, where the coefficients of A and B relate to yield strength and strain-hardening modulus, but it cannot represent the influence of material microstructure and size effect on the quasi-static flow stress. For the second term, the effect of strain rate on flow stress is addressed through introducing strain rate coefficient C. The third term represents the influence of working temperature, andT_m,T_0, and T_w denote the melting temperature, room temperature, and working temperature, respectively. p and q are the coefficients relating to strain hardening and thermal softening, respectively. ε_0 is reference plastic strain rate equaling to 1.

Generally, Johnson–Cook constitutive equation is limited to estimate the flow stress in macroscopic plastic deformation. For example, difficult-to-eliminate deviation will generate when Johnson–Cook equation is used as the stress–strain fitting formula for micro/nanoscopic plastic deformation [16]. Therefore, the $A + B\varepsilon^{p}$ term in Johnson–Cook equation is replaced by Eq. (15) in this study, to correlate the material microstructure and size effect to the flow stress estimation. Besides, another size effect coefficient D is also imported to amend strain rate with respect to size effect. With the assistance of the well-known Von Mises Criterion, the equivalent flow stress (τ_s), strain (γ_s), and strain rate $(\dot{\gamma}_s)$ in cutting region can be related to the flow stress (σ), strain (ε), and strain rate $(\dot{\varepsilon})$ in Johnson–Cook equation. Thus, the constitutive relation of polycrystalline metals in micro/nano-deformation is expressed as

$$\tau_s = \frac{1}{\sqrt{3}}\left[\left(Mk_R\left(\frac{\gamma_s}{\sqrt{3}}\right)^{n} + \alpha_d\mu_p b_v\sqrt{\frac{C_1\gamma_s}{\sqrt{3}b_v D}}\right) - \eta\left(Mk_R\left(\frac{\gamma_s}{\sqrt{3}}\right)^{n} + \alpha_d\mu_p b_v\sqrt{\frac{C_1\gamma_s}{\sqrt{3}b_v D}} - mk_R\left(\frac{\gamma_s}{\sqrt{3}}\right)^{n}\right)\right] \left[1 + Cln\left(\frac{\dot{\gamma}_s}{\sqrt{3}}\right)\right]\left[1 + D'ln\left(\frac{\eta}{\eta_0}\right)\right]\left[1 - \left(\frac{T_w - T_0}{T_m - T_0}\right)^{q}\right] \quad (17)$$

where η_0 is the reference size factor for macroscopic deformation. According to the velocity vector relation of shear band, the strain $(\gamma_s^{i,j})$ in the shear band for the j-th discrete element at the i-th rotational angle can be assumed as a constant value and expressed as

$$\gamma_s^{i,j} = \frac{cos\gamma_e^{i,j}}{2sin\phi_{i,j}cos\left(\phi_{i,j} - \gamma_e^{i,j}\right)} \quad (18)$$

where $\gamma_e^{i,j}$ and $\phi_{i,j}$ represent the equivalent rake angle and shear angle. The corresponding strain rate $(\dot{\gamma}_s^{i,j})$ can be estimated by adopting the empirical expression proposed by Oxley and Hastings [27], whose availability has been proven in the force modelling for micro-cutting process and can be expressed as

$$\dot{\gamma}_s^{i,j} = \frac{C_0 v_{sh}^{i,j}}{l_{AB}^{i,j}} = \frac{C_0 v_{sh}^{i,j} sin\phi_{i,j}}{t_c^{i,j}} \quad (19)$$

where C_0 is the factor that relates to the material property and cutting condition. $l_{AB}^{i,j}$ is the length of the straight shear band. According to the geometrical relation in Fig. 4, the velocity along the shear band $(v_{sh}^{i,j})$ is formulated as

$$v_{sh}^{i,j} = \frac{cos\gamma_e^{i,j}}{cos\left(\phi_{i,j} - \gamma_e^{i,j}\right)}v = \frac{\pi S_v S_w cos\gamma_e^{i,j}}{30cos\left(\phi_{i,j} - \gamma_e^{i,j}\right)} \quad (20)$$

where v denotes the cutting speed. In micro/nano-cutting, the extreme small UDCT makes the equivalent rake angle to be highly negative. The original round tool edge can be replaced by an equivalent tool rake face, though drawing a straight line between the points A and C as shown in Fig. 4. Point A is the contact point between the bottom of the tool edge and the machined surface, and point C located on tool rake face is the mark point of the equivalent tool-chip contact length. Thus, based on the geometrical relation, the equivalent rake angle $(\gamma_e^{i,j})$ at a specific UDCT can be determined by

$$\gamma_e^{i,j} = \gamma_0 + \arctan\left(\frac{u_{i,j}}{\zeta t_c^{i,j}}\right) \quad (21)$$

$$u_{i,j} = \begin{cases} r_e\cos\gamma_0 - \frac{\zeta t_c^{i,j} - r_e}{\cos\gamma_0} & t_c^{i,j} \geq \frac{r_e(1+\sin\gamma_0)}{\zeta} \\ r_e\cos\left(\arcsin\left(\frac{r_e - \zeta t_c^{i,j}}{r_e}\right)\right) & else \end{cases} \quad (22)$$

where r_e denotes the tool edge radius and γ_0 is the tool rake angle. ζ is the coefficient that determines the equivalent tool-chip contact length.

Shear angle is jointly influenced by the cutting condition and the material property. Especially in micro/nano-cutting, the impact of crystal anisotropy on shear angle cannot be neglected, because the tool-workpiece normally interacts within a single crystal. Wang et al. [28] demonstrated that

the activated dislocation slip system in the primary deformation zone depends on the relative angle between the cutting direction and the crystal orientation. Thus, to address the crystal anisotropy, a modified shear angle equation is proposed in this study by incorporating Taylor factor (M), which is normally used as an approximate measure of the relative direction of dislocation sliding activities to the crystal orientation, into Lee's shear angle equation as

$$\phi_{i,j} = (aM + b)\left(\frac{\pi}{4} + \gamma_e^{i,j} - \beta\right) \tag{23}$$

where a and b are the constant for the linear relation, which can be derived by curve fitting method. β denotes the friction angle.

The working temperature ($T_w^{i,j}$) in the deformation zone is required to be estimated before calculating flow stress using Eq. (17). As it is difficult to accurately measure the working temperature using experimental methods, analytical models are generally regarded as an alternative way. Even though finite element methods have been reported to determine the temperature distribution in micro/nano-cutting process, these models can greatly complicate the force model [29, 30]. To improve the modelling efficiency, a simplified temperature model is proposed in this study on the basis of the model proposed by Boothroyd et al. [31], to calculate the working temperature, and it can be expressed by

$$T_w^{i,j} = T_0 + \frac{2\left(1-\beta'\right)\gamma_s^{i,j}\tau_s}{\rho S_T} \tag{24}$$

where β' denotes the heat dissipation coefficient, ρ is the density of the workpiece material, and S_T is the specific heat. This proposed temperature estimation model fully considers the plastic deformation heat, thermal diffusion, and heat convection. By incorporating Eq. (18), Eq. (19), and Eq. (24) into the Eq. (17), the shear flow stress that acts parallel to the shear band can be analytically determined for UPFG.

2.2.2 Calculation of nominal and frictional cutting force

The cutting force is essentially generated by the interactions between tool rake face and chip, so the distribution of flow stress at the secondary deformation zone (tool-chip interface) needs to be determined before calculating the nominal cutting force and frictional cutting force. As shown in Fig. 5, according to the stress equilibrium relation in the shear band, the change rate of hydrostatic stress along the straight line AB can be expressed by

$$\frac{\partial\sigma}{\partial s_1} = \frac{\partial\tau}{\partial s_2} = \frac{\partial\tau}{\partial\gamma}\frac{\partial\gamma}{\partial t}\frac{\partial t}{\partial s_2} + \frac{\partial\tau}{\partial\dot{\gamma}}\frac{\partial\dot{\gamma}}{\partial s_2} + \frac{\partial\tau}{\partial T_w}\frac{\partial T_w}{\partial s_2} \tag{25}$$

where s_1 and s_2 are the distance parallel and vertical to the shear band. The temperature gradient is small enough to be neglectable in diamond cutting, and the strain rate can be assumed to approach the maximum value at the shear band [4]. Thus, the second term and the third term are assumed to be equal to zero, and the hydrostatic stress at point A can be calculated by integral method as

$$\sigma_A^{i,j} = \sigma_B^{i,j} + \frac{t_c^{i,j}}{v_\perp sin\phi_{i,j}}\frac{\partial\tau_s}{\partial\gamma_s^{i,j}}\dot{\gamma}_s^{i,j} \tag{26}$$

where $v_\perp$ is the velocity vertical to the shear band equal to $vsin\phi_{i,j}$ and the term $\frac{\partial\tau_s}{\partial\gamma_s^i}$ can be obtained through conducting differential algorithm on Eq. (17).

As the cutting direction is nearly parallel to the surface formed by previously rotary cutting, the boundary condition

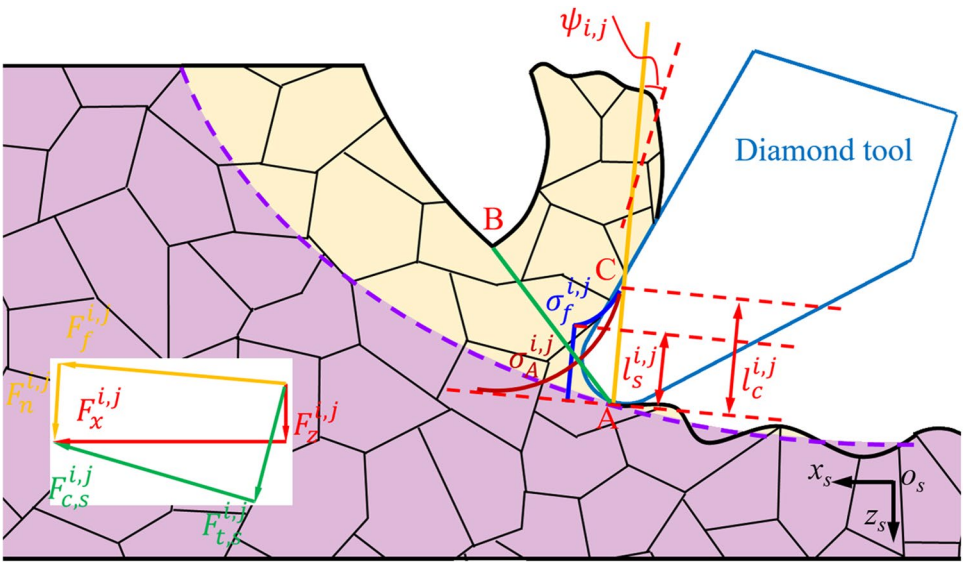

Fig. 5 Schematic of the distribution of normal and frictional stress at tool-chip interface

of flow stress can be obtained by Oxley's approximate cutting theory, in which the strain, strain rate, and temperature along line AB are assumed to be constant. Thus, the change rate of the hydrostatic stress along shear band is also constant according to Eq. (25), and another expression between the hydrostatic stress of point A and point B can be expressed by

$$\sigma_A^{i,j} + \sigma_B^{i,j} = 2\tau_s \tan(\varsigma) \tag{27}$$

where is ς the angle between the resultant force and shear band, which can be estimated by referring [32] as

$$\tan(\varsigma) = 1 + 2\left(\frac{\pi}{4} + \phi_{i,j}\right) - \frac{t_c^{i,j}}{2\tau_2 \sin\phi_{i,j}} \frac{\partial \tau}{\partial s_2} \tag{28}$$

Through integrating Eq. (27) into Eq. (26), the hydrostatic stress of point A ($\sigma_A^{i,j}$) and point B ($\sigma_B^{i,j}$) can be determined. According to the thermal–mechanical model proposed by Cheng et al. [23], the normal stress ($\sigma_n^{i,j}$) at the equivalent tool-chip interface exponentially decreases from the highest value at point A to zero at the tool-chip separation point C, as the yellow line shown in Fig. 5. Accordingly, the distribution of the normal stress at equivalent tool-chip interface can be expressed as

$$\sigma_n^{i,j}(s) = \sigma_A^{i,j}\left[1 - \left(\frac{s}{l_c^{i,j}}\right)^{\xi}\right] \tag{29}$$

where s denotes the coordinate along equivalent tool rake face with respect to point A and ξ is the coefficient that characterizes the shape of the stress distribution. $l_c^{i,j}$ denotes the tool-chip contact length. It is worth to note that the equivalent tool-chip interface is defined as the straight line connecting the bottom of the cutting edge (point A) and the tool-chip separation point (point C). According to the momentum equilibrium, the contact length $l_c^{i,j}$ can be expressed by

$$l_c^{i,j} = \frac{2+r}{r} \frac{t_c^{i,j} \cos\left(\phi_{i,j} + \beta - \gamma_e^{i,j}\right)}{\sin\phi_{i,j}\cos\beta} \tag{30}$$

In diamond cutting, the tool-chip contact state is very complicated featuring discontinuous frictional states of sticking and sliding, as shown in Fig. 5. Specifically, in the region near the bottom of cutting edge, the high normal stress exerted on the tool leads to the sticking friction state with constant frictional stress. With the decrease of the normal stress in the region near the tool-chip separation point, the frictional state transfers to the sliding govern by the Coulomb friction law. Even though the hybrid analytical–numerical models are high qualified for the estimation of the discontinuous frictional state at tool-chip interface, these models can reduce the efficiency of the cutting force model. Besides, it is still difficult for current analytical models to determine the location of the transfer point from sticking the sliding. Thus, a simplified tool-chip contact model is proposed in this study to efficiently estimate the discontinuous distribution of the frictional stress ($\sigma_f^{i,j}$) at tool-chip interface, which is expressed as

$$\sigma_f^{i,j}(s) = \begin{cases} \mu_f \sigma_A^{i,j}\left[1 - \left(\frac{l_s^{i,j}}{l_c^{i,j}}\right)^{\xi}\right] & 0 \le s < l_s^{i,j} \\ \mu_f \sigma_n^{i,j}(s) & l_s^{i,j} \le s < l_c^{i,j} \end{cases} \tag{31}$$

where μ_f is the friction coefficient and $l_s^{i,j}$ denotes the length of sticking region. According to the model, frictional stress is increasing when approaching to the bottom of the cutting edge. Based on the plastic deformation criterion [27], the frictional stress should be no larger than the hydrostatic stress at the exit of the shear band (point B). Accordingly, the length of the sticking region can be obtained by the following expression as

$$l_s^{i,j} = l_c^{i,j}\left(1 - \frac{\sigma_A^{i,j}}{\mu_f \sigma_B^{i,j}}\right)^{\frac{1}{\xi}} \tag{32}$$

Through integration method, the nominal cutting force and frictional cutting force for the orthogonal cutting element at the j-th discrete element of the i-th rotational angle can be estimated as

$$\begin{cases} F_n^{i,j} = \int_0^{l_c^{i,j}} w_i \sigma_n^{i,j}(s) ds \\ F_f^{i,j} = \int_0^{l_c^{i,j}} w_i \sigma_f^{i,j}(s) ds \end{cases} \tag{33}$$

Overall, the cutting force and thrust force for the orthogonal cutting element at the j-th discrete element of the i-th rotational angle can be obtained by coordinate transformation as

$$\begin{cases} F_{c,s}^{i,j} = F_n^{i,j}\sin\psi_{i,j} + F_f^{i,j}\cos\psi_{i,j} \\ F_{t,s}^{i,j} = F_n^{i,j}\cos\psi_{i,j} - F_f^{i,j}\sin\psi_{i,j} \end{cases} \tag{34}$$

where $\psi_{i,j}$ is the induced angle between the equivalent tool rake face and vertical direction and can be determined according to the geometrical relation in Fig. 5 as

$$\psi_{i,j} = \begin{cases} \arccos\left(\frac{l_c^{i,j}}{2r_e}\right) & l_c^{i,j} < 2r_e \sin\left(\frac{\pi}{4} + \frac{\gamma_0}{2}\right) \\ \arcsin\left(\frac{r_e + r_e\sin\gamma_0}{l_c^{i,j}}\right) - \gamma_0 & else \end{cases} \tag{35}$$

2.3 Rubbing force model for elastic recovery

In case that the UDCT is lower than the critical uncut chip thickness, high negative rake angle occurs, leading to the

transition from material plastic separation (cutting) to material elastic deformation (rubbing). In this case, the workpiece material is extruded beneath the tool edge similar to indentation operation, as illustrated in Fig. 6. Accordingly, the rubbing force can be assumed to be proportional to the interference volume between the cutting edge and workpiece. With the consideration of the tool geometry and the width of discrete element, the interference volume ($\Lambda_{i,j}$) can be calculated as

$$\Lambda_{i,j}=\begin{cases} 2w_i r_e \arccos\left(\frac{r_e-t_c^{i,j}}{r_e}\right) & t_c^{i,j}\le r_e(1-\cos\kappa) \\ w_i r_e \arccos\left(\frac{r_e-t_c^{i,j}}{r_e}\right)+r_e\kappa+\frac{t_c^{i,j}-r_e(1-\cos\kappa)}{\sin\kappa} & r_e(1-\cos\kappa)<t_c^{i,j}\le d_c \end{cases} \tag{36}$$

where d_c denotes the critical DoC and is assumed to be $0.25r_e$ [12]. The rubbing force induced by the material elastic deformation in cutting direction ($F_{c,r}^{i,j}$) and thrust direction ($F_{t,r}^{i,j}$) for the orthogonal cutting element at the j-th discrete element of the i-th rotational angle can be expressed by

$$\begin{cases} F_{c,r}^{i,j}=\mu_r\Lambda_{i,j}k_r \\ F_{t,r}^{i,j}=\Lambda_{i,j}k_r \end{cases} \tag{37}$$

where μ_r denotes the friction coefficient of rubbing and k_r is the rubbing force coefficient that can be determined by assuming that the rubbing force and cutting force is continuous at critical chip thickness.

2.4 Calculation of cutting force for UPFG

As discussed above, the cutting force of UPFG consists of two parts, namely, impulse cutting force and free-vibration force.

2.4.1 Calculation of impulse cutting force

The impulse cutting force is generated by the short but continuous cutting process at tool-workpiece contact duration. By summarizing the force components of all the discrete elements as expressed in Eq. (34) and Eq. (37), the overall cutting force and thrust force at the i-th rotational angle (θ_i) and j-th discrete angle (φ_j) can be expressed by

$$\begin{cases} F_c^{i,j}=\sum\left\{F_{c,r}^{i,j}|\forall t_c^{i,j}<d_c\right\}+\sum\left\{F_{c,s}^{i,j}|\forall t_c^{i,j}\ge d_c\right\} \\ F_t^{i,j}=\sum\left\{F_{t,r}^{i,j}|\forall t_c^{i,j}<d_c\right\}+\sum\left\{F_{t,s}^{i,j}|\forall t_c^{i,j}\ge d_c\right\} \end{cases} \tag{38}$$

As illustrated in Fig. 5, the direction of cutting force and thrust force changes with tool rotation, while the dynameter can only capture the cutting force signals in vertical (z_s) and horizontal (x_s) directions. By coordinate transformation, the cutting forces in vertical (z_s) and horizontal (x_s) directions can be expressed by

$$\begin{cases} F_x^{i,j}=F_c^{i,j}\cos\theta_i+F_t^{i,j}\sin\theta_i \\ F_z^{i,j}=-\left(F_c^{i,j}\sin\theta_i+F_t^{i,j}\cos\theta_i\right) \end{cases} \tag{39}$$

2.4.2 Calculation of free-vibration force

In UPFG, the workpiece is generally fixed on the force sensor to capture cutting force signals. Due to the elastic property of the sensitive element (piezoelectric ceramics) of the force sensor, the periodic impulse cutting force can lead to the free-vibration forces coupled into the force signal. The workpiece together with the force sensor are modeled by a second-order mass-spring-damping system in this study to

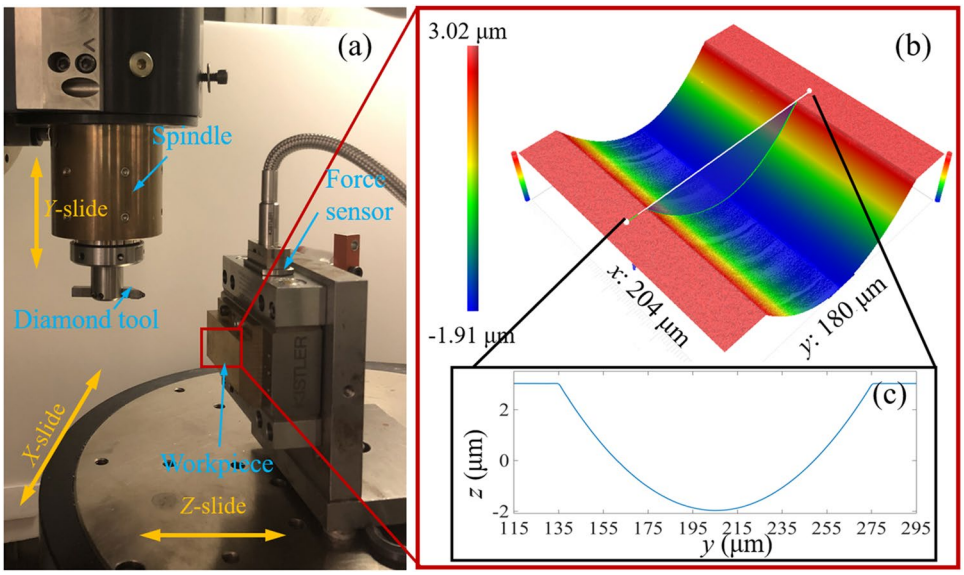

Figure 6. **a** Experiment setup and **b** the micro-topography of the machined micro-groove and **c** the corresponding cross-sectional profile.

approximately estimate the vibration-free forces. Thus, the dynamic equation of the system along horizontal (x_s) and vertical (z_s) directions can be expressed by

$$\begin{cases} \frac{d^2x}{dt^2} + 2\zeta'\omega_n\frac{dx}{dt} + \omega_n^2 x = 0 \\ \frac{d^2z}{dt^2} + 2\zeta'\omega_n\frac{dz}{dt} + \omega_n^2 z = 0 \end{cases} \tag{40}$$

where ζ' is the damping ratio and ω_n is the oscillation frequency without damping.

It is known that for any elastic components, the force signal is proportional to the displacement within the measurement range. Accordingly, by solving Eq. (40), the vibration-free forces stimulated by F_x^v and F_z^v can be expressed by

$$\begin{cases} F_x^v = \frac{max\left(F_x^{i,j}\right)}{\sqrt{1-\zeta'^2}} e^{-\zeta\omega_n t} sin\left(\omega_d t + \vartheta\right) \\ F_z^v = \frac{max\left(F_z^{i,j}\right)}{\sqrt{1-\zeta'^2}} e^{-\zeta\omega_n t} sin\left(\omega_d t + \vartheta\right) \end{cases} \tag{41}$$

where ω_d is the oscillation frequency equaling to $\omega_n\sqrt{1-\zeta'^2}$ and ϑ is the damping angle equaling to $\arccos\left(\zeta'\right)$. Overall, the cutting forces for UPFG can be calculated by solving Eqs. (39) and (41).

3 Experiment setup and procedure

To validate the proposed force model, fly grooving experiments were conducted in this study using 5-axis ultra-precision milling machine (Precitech 705G), as shown in Fig. 6a. The workpiece with plane surface is screwed on the force sensor and then configured on the rotational table (C-axis). A single point diamond tool with the nose radius of 0.5 mm is mounted on the high-speed spindle. The cutting edge radius of the diamond tool is 40 nm, and the rake angle and the clearance angle of the tool are 0° and 7°, respectively. Through the feed motions of the rotational diamond tool along *X*-slide with a specific depth of cut, micro-grooves can be fabricated. The cross-sectional profile of the micro-groove is perfectly the same with the shape of the cutting edge of the diamond tool, as shown in Fig. 6 b and c. The shape of the micro-groove can be flexibly tuned by changing the depth of cut and tool edge shape.

According to the kinematics of UPFG, it is learned that the dominant machining parameters in UPFG includes feed rate, depth of cut, and swing radius. To fully validate the proposed force model and to study the influence of different machining parameters on cutting force, three groups of machining parameters were employed, as listed in Table 1. The spindle speed is set at 4000 rpm in the experiments. To capture the cutting force signal, a three-axial dynameter (Kistler Group 9255b) was employed in the experiments. Besides, the experiments were conducted under dry cutting condition, and the sample frequency of the dynameter is set at 30 kHz, improving the measurement accuracy. After cutting experiments, the formed chips are collected and observed by scanning electron microscope (SEM), to study the cutting mechanism transformation phenomenon in UPFG. Polycrystalline copper, a typical material used in optical mold, is used as the workpiece material in this study. To determine the influence of microstructure on the cutting force, the workpiece material is etched and observed using an optical microscope (BX60, Olympus corporation) to measure the average grain size. The average grain size of the polycrystalline copper is measured at about 28 μm.

4 Results and discussion

In this section, the transformation of cutting mechanism in UPFG with trans-scale chip thickness variation is analyzed by correlating the simulation results of the proposed model and the observed chip morphologies. This can provide an insight understanding of the unique cutting mechanism of UPFG as well as can validate the proposed HSLM. Besides, the effectiveness of the proposed cutting force model for UPFG is validated by comparing the estimated forces and the experimental results in UPFG of polycrystalline copper with different machining parameters.

4.1 Trans-scale cutting mechanism transformation in UPFG

According to the model introduced in Sect. 2.1, the simulated chip morphology and the corresponding cross-sectional profiles at different rotational angles are shown in Fig. 7 a and b, respectively. It is observed that the unique kinematics of UPFG results in the axisymmetric chip morphology featuring ever-changing shape of the cross-sectional profiles with tool rotation. To accurately estimate the cutting force, each cross-section is further evenly discretized by a very small angle of 0.1°, and each discrete element is treated as an independent orthogonal cutting process with corresponding local UDCT. The changes of the UDCT for the discrete cross-sections are shown in Fig. 7c. It is seen in Fig. 7c that the UDCT decreases from the middle to the two sides, and

Table 1 Machining parameters of UPFG

Group	Feed rate (mm/r)	Depth of cut (μm)	Swing radius (mm)
1	0.04, 0.06, 0.08, 0.1, 0.12	8	30
2	0.1	4, 6, 8, 10, 12	30
3	0.1	8	25, 30, 35, 40, 45

the maximum chip thickness reaches at the middle of the cross-sections due to the asymmetric chip morphology. This is attributed to that each chip is formed by two successive cutting processes of the rotational diamond tool with a fixed swing radius, as illustrated in Fig. 2a. Thus, it is learned that the local UDCT of each discrete orthogonal cutting element is jointly dependent on its position on the tool edge and the rotational angle. Noteworthy, as shown in Fig. 7d, the maximum chip thickness of the cross-sections firstly increases and then decreases with tool rotation, featuring a trans-scale variation between nanoscale to microscale.

As shown in Fig. 8a, size factor (SF) is defined as the ratio of the grain size to UDCT sharply decreases and then increases with tool rotation in UPFG, due to the trans-scale variation of chip thickness within each tool rotational cycle. This variation trend is corresponding to the change of the average UDCT shown in Fig. 7d. The larger value of SF indicates that less crystals are included in the cutting region, in which case the influence of microstructure factors (i.e., grain size, grain boundary, crystallographic anisotropy, microcracks, dislocation density) on material micro-mechanics properties becomes increasingly prominent during material plastic deformation, similar to nano-cutting of single crystals [33]. Besides, as learned for "Surface layer model," the surface grains in the cutting region suffer less deformation resistance than that of internal grains. This is due to the fact that the few dislocations pile up at free surface, further leading to lower flow stress in the deformation zone under large SF. In contrast, according to the definition of SF, smaller SF means that more crystals are included in the cutting region, similar to micro-cutting of polycrystal. The large variation of SF in UPFG indicates the obvious transformation of the cutting states between nano-cutting and micro-cutting.

To further elucidate the SF related cutting mechanism transformation in UPFG, the chip morphologies formed in UPFG of polycrystalline copper are analyzed by SEM with different magnification times, as shown in Fig. 9. The observed chip morphology shown in Fig. 9a is axisymmetric and similar to the simulated chip morphology shown in Fig. 7a, validating the effectiveness of the chip model. As shown in Fig. 9 b and c, the micro-topographies of the two different regions of the chip, namely, region 1 and region 2, are also observed using a larger magnification time. Interestingly, two significantly different micro-topographies are observed at two different regions. As shown in Fig. 9b, the micro-topography at region 1 is very smooth without lamella-like structures, indicating that the material is removed by ploughing mechanism (compressive stress) induced plastic deformation [28, 33]. As learned from Fig. 8a, very high SF values are reached at region 1, in which case the diamond tool cuts within a single or only a few crystals. The less deformation resistance of grain boundary in this case is more beneficial to formation of smooth and thin chips [34]. Besides, according to the HSLM, the equivalent rake angle of the diamond tool edge is negative at very small UDCT, further resulting in the continuous plastic deformation of the material under high compressive stress (ploughing). In contrast, intensive and large lamella-like structures are observed at region 2, as pointed by the red arrows in Fig. 9c. As the UDCT at region 2 increases to a few micrometers, the SF value is very small, and the cutting process is closer to macro-cutting process. Accordingly, the lamella-like structures are generated by the adiabatic shear band (ASB)-dominated material removal mechanism under tensile stress (shearing mechanism) [34]. Overall, it is learned that the trans-scale variation of UDCT in UPFG

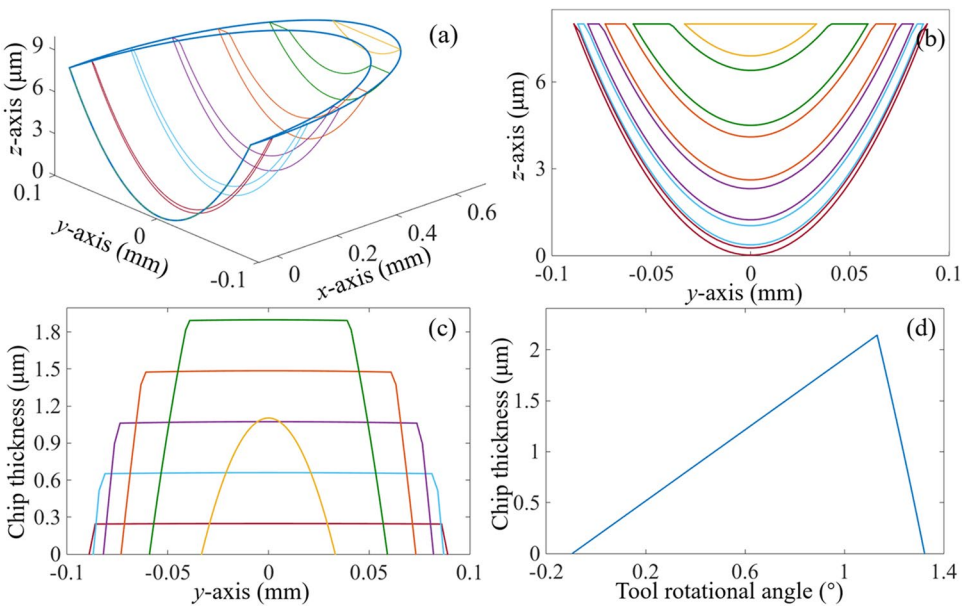

Fig. 7 The simulated results of the **a** chip morphology, **b** cross-sectional profiles at different rotational angles, **c** the corresponding chip thickness of each cross-section, and **d** chip thickness variation with tool rotation

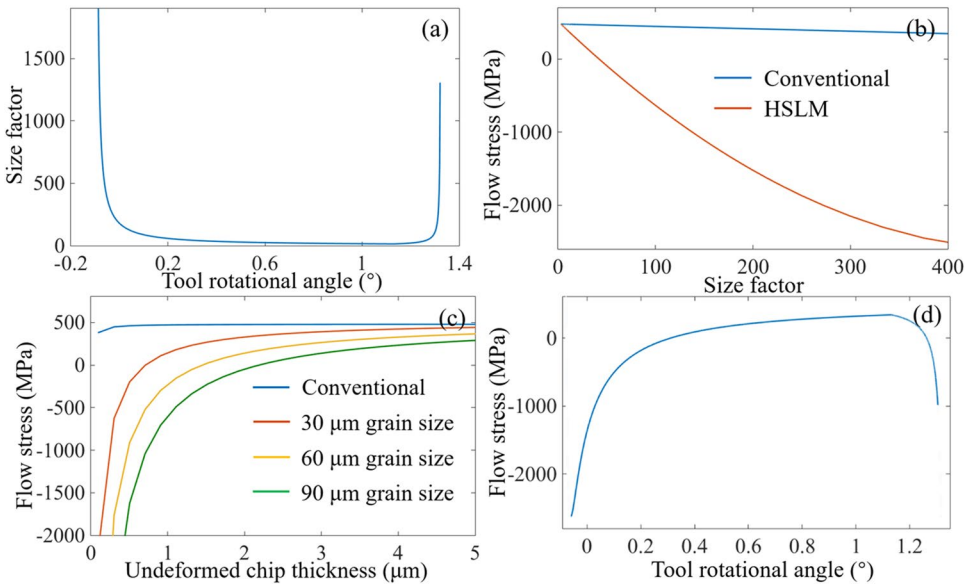

Fig. 8. **a** The variation of size factor with tool rotation, a comparison of the estimated flow stress between conventional model and the proposed HSLM with the change of **b** size factor and **c** UDCT and **d** the variation of flow stress with tool rotation in UPFG.

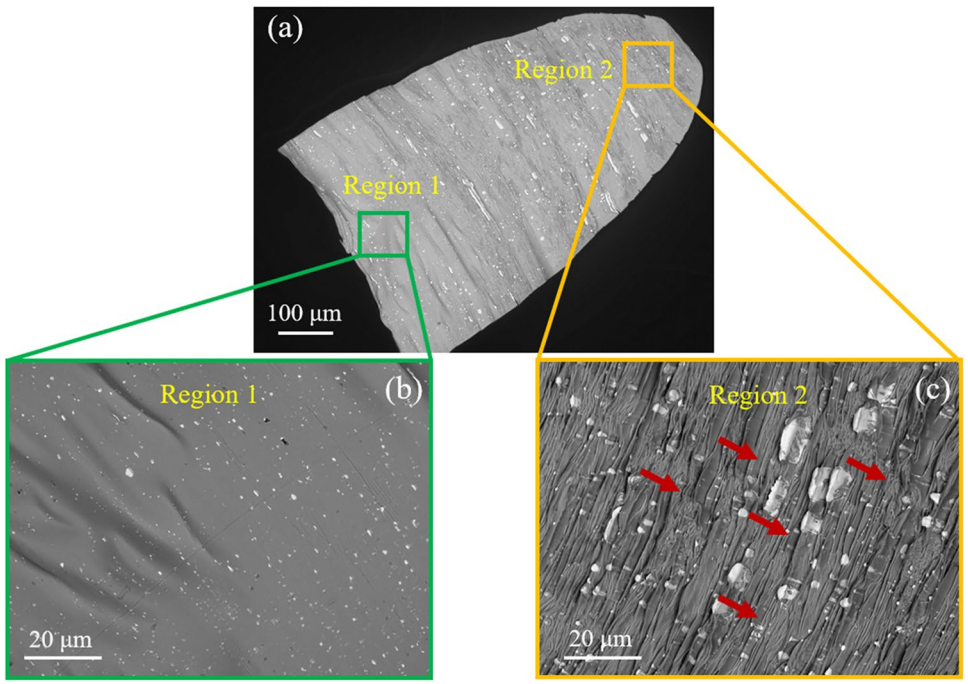

Fig. 9 The formed chip morphology and the micro-topographies at different positions

results in the alternative transformation of cutting mechanism between ploughing (compressive stress) and shearing (tensile stress).

Noteworthy, conventional slip-line models used for micro/nano-cutting force estimation are generally developed by simply incorporating the effective rake angle into the macroscope slip-line models, and Johnson–Cook constitutive equation is normally employed to calculate flow stress [4, 12]. As shown in Fig. 8b, the flow stress calculated by the conventional slip-line models is almost unchanged and remains in positive values (tensile stress) with the decrease of UDCT, which cannot well explain the cutting mechanism transformation phenomenon in UPFG as observed in the different chip morphologies shown in Fig. 9. In comparison, by fully considering the equivalent negative rake angle as well as the microstructure and size effect, the proposed HSLM can well estimate the transition of flow stress from tensile (shearing) to compressive (ploughing) with the increase of SF, as comparatively shown in Fig. 8b. According to microforming theory, the flow stress in UPFG is jointly influence by the flow stress of surface grains (σ_s) and inner grains (σ_i). Noteworthy, the influence proportion of σ_s or σ_i on the total flow stress is determined by the size factor, according to Eq. (11).

A further comparison of the proposed HSLM and conventional slip-line model in estimating the variation of flow stress with respect to UDCT and grain size is shown in Fig. 8c. It is seen that compared with the conventional slip-line models, the flow stress calculated by HSLM increases from negative values (compressive stress) to positive values (tensile stress) with increase of UDCT. Besides, the flow stress calculated by the HSLM decreases with the increase of grain size, due to the less grain boundary resistance during dislocation sliding for larger grains [33]. Considering the uneven grain size of the workpiece material, the average grain size of the workpiece is measured in advance by optical microscope before cutting force estimation. According to [33, 35], in spite of the uneven grain size of polycrystalline metals, the average grain size statistically determines the mechanical properties of the during plastic deformation. Based on crystal plasticity theory, total dislocation density ρ_T in Eq. (13) can be used to represent the influence of random dislocations on flow stress in the cutting region. In the proposed cutting force model, Eq. (13) is used to determine the flow stress in the cutting region. Accordingly, it is learned that grain size and random dislocations influence the flow stress in the cutting region, thereby affecting the cutting forces of UPFG. The simulation results validate that the proposed HSLM can well capture the influence of size effect and grain size on flow stress. To further validate the HSLM, the changes of the flow stress with respect to tool rotational angle are also determined by the proposed HSLM, as shown in Fig. 8d. It is learned that the flow stress changes from compressive to tensile and then back to compressive with tool rotation. The simulation result agrees well with the chip morphologies observed in Fig. 9, validating the effectiveness of proposed HSLM on capturing the UDCT related cutting mechanism transition phenomenon in UPFG.

4.2 Validation of the cutting force model for UPFG

To validate the proposed force model, the estimated forces are compared with the measured forces in UPFG of polycrystalline copper using different machining parameters, as listed in Table 1. Through summarizing the parameters in [10, 33, 36], the parameters relating to the physical characteristics of polycrystalline copper and Johnson–Cook constitutive equation in the model are determined, as shown in Table 2. It is known that for single crystal metals, the Taylor factor with respect to one specific crystal orientation can be calculated according to its definition by referring [37]. Nevertheless, due to the randomness of the crystal orientation of the grains for polycrystalline metals, it is hard to accurately determine the Taylor factor by measuring the crystal orientation of all grains. Considering the fact that a few grains with different crystal orientations may simultaneously contact the diamond tool along cutting edge in UPFG, the Taylor factor of polycrystalline copper (FCC polycrystals) is assumed to be 3.06 by referring [19, 33, 38]. The availability of these parameters has been validated using physical experiments by researchers. The remaining parameters listed in Table 3 are determined and optimized by training method, in which the cutting forces collected with the feed rate of 0.06 mm/r, DoC of 7 μm, and spindle speed of 4000 rpm were used as learning material. Specifically, these parameters are reasonably preset in advance, and then generation algorithm is employed to optimize these parameters based on the collocated original cutting force signals.

Taking one set of machining parameters (feed rate of 0.1 mm/min, DoC of 8 μm, and swing radius of 30 mm) as an example, a comparison of the estimated and measured cutting forces in *x*-axis and *z*-axis directions are shown in Fig. 10. Both of the estimated and the measured cutting forces include two parts, namely, impulse cutting force and free-vibration force. It is worth to note that only the first impulse of the cutting force signal is the real cutting force, while the subsequent and gradually attenuated impulses are the free-vibration forces of force sensor. Different from conventional cutting, UPFG features a very short tool-workpiece contact duration at each tool rotational cycle, and most proportion of each tool rotational cycle is idling. Accordingly, the sampling frequency for UPFG should be high enough in cutting force measurement, to collect the impulse cutting force (the first impulse of the force signal). It is observed that the free-vibration section of the measured cutting forces is not a perfect impulse response signal of second-order dynamic system, as shown in Fig. 10 c and

Table 2 Parameters related to material mechanics properties

D'	46.5	k_R	196
q	0.22	n	0.26
M	3.06	m	2
α_d	0.34	T_m	1084 °C
μ_p	78,500 MPa	b_v	2.608×10^{-10} m
ρ	8.9 g/cm^3	T_0	25 °C
S_T	445 J/kg·°C	β'	0.35
C_1	0.11	D	24 μm

Table 3 Parameters related to the analytical model

γ_0	0°	C_0	6
$\Delta\theta$	2°	ζ	1.7
$\Delta\varphi$	1°	a	0.129
β	15°	b	0.216
r	3	ξ	0.56
μ_f	0.084	κ	7°
μ_r	0.18	R_t	0.5 mm
r_e	40 nm	ζ’	0.03

d. This is properly attributed to the coupling effect of the sensitive elements of the force sensor as well as the influence of the mass of the workpiece. It is worth to note that the free-vibration force is merely the impulse response of the force sensor, while the impulse section of the cutting force signal essentially reflects the tool-workpiece interactions. The reason of the periodic positive and negative values of the free-vibration forces is that the sensitive element (piezoelectric ceramics) of the force sensor periodically vibrates around its equilibrium position (0 N in this position), after the periodically short and heavy impact of the diamond tool, as illustrated in Fig. 1c.

As the shape of the impulse cutting forces cannot be clearly observed in Fig. 10, an enlarged view of the impulse cutting forces (the first impulse of the cutting force signal) in both x- and z-axis directions is shown in Fig. 11. The estimated cutting forces and the measured cutting forces present a good accordance with each other at different tool rotational angle, validating the effectiveness of the proposed model. Even though there exists a trans-scale variation of the UDCT between nanoscale and microscale, the maximum estimation errors for the impulse cutting force in x-axis and z-axis directions are very small at about 0.05 N and 0.01 N, respectively. The small estimation errors are majorly attributed to the full consideration of the equivalent negative rake angle, microstructure of polycrystalline metals, and size effect in the proposed HSLM, so the force model can well capture the cutting mechanism transformation in UPFG. Besides, compared with conventional force models, more coefficients relating to material micro-mechanics properties are involved in the proposed HSLM to improve the estimation accuracy.

Generally, the maximum estimation error of impulse cutting forces generates at the same time when the cutting forces reaches the maximum values as point c in Fig. 3. Thus, to further validate the cutting force model, the estimated results of the maximum values of impulse cutting forces at different machining parameters are compared with the measured ones, as shown in Fig. 12. The estimation errors of the cutting forces in x-axis and z-axis directions are mostly lower than 0.04 N at different machining parameters, validating effectiveness of the proposed force model on well capturing the influence of the machining parameters on cutting forces in UPFG. It is interesting to observe that apart from the swing radius, the cutting forces increases with the increase of the machining parameters, i.e., feed rates and DoC. This attributes to the fact that the chip thickness decreases with increase of the swing radius, while increases with increases other machining parameters.

According to the proposed model and experimental results, the generation mechanism of cutting forces for UPFG is jointly influenced by kinematics, chip formation, material microstructure, material elastic recovery, size effect, and tool geometry. Specifically, the kinematics and tool geometry jointly influence the chip morphology of UPFG and cross-sections of the chip at each tool rotational angle, as shown in Fig. 7 and Fig. 9a, thereby influencing the amplitude and shape of impulse cutting forces. The estimated impulse cutting forces shown in Fig. 11 are calculated based on the simulated chip morphology shown in Fig. 7. A good accordance is achieved between the simulated and

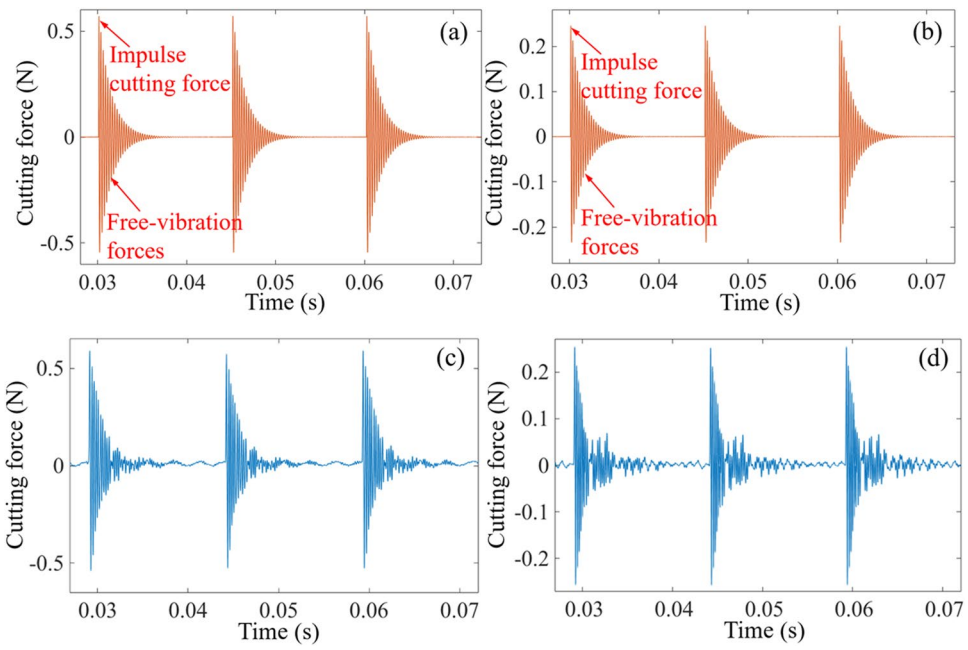

Fig. 10 The estimated force in **a** x-axis direction and **b** z-axis direction, and the measured force in **c** x-axis direction and **d** z-axis direction

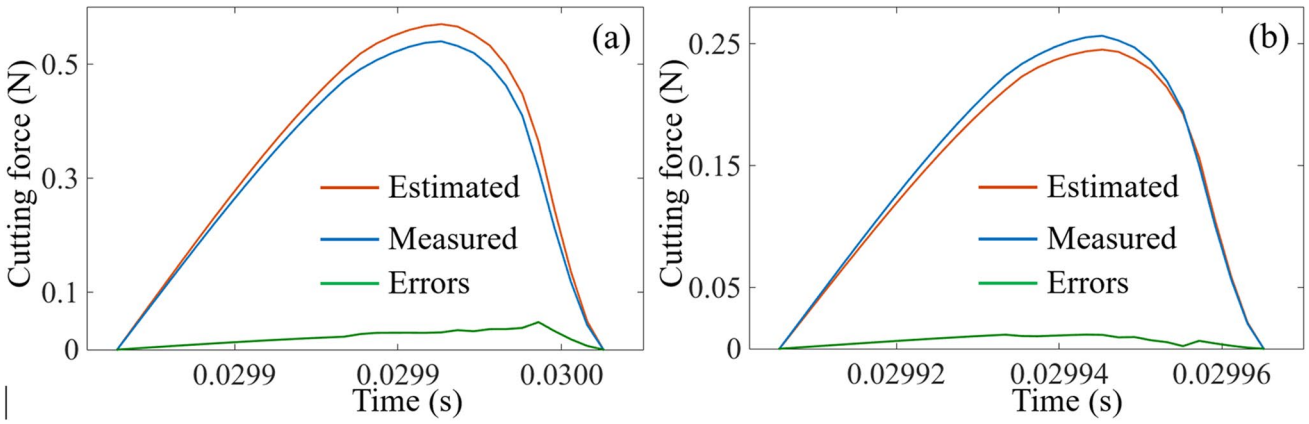

Fig. 11 A comparison of the estimated and measured impulse cutting in **a** x-axis direction and **b** z-axis direction

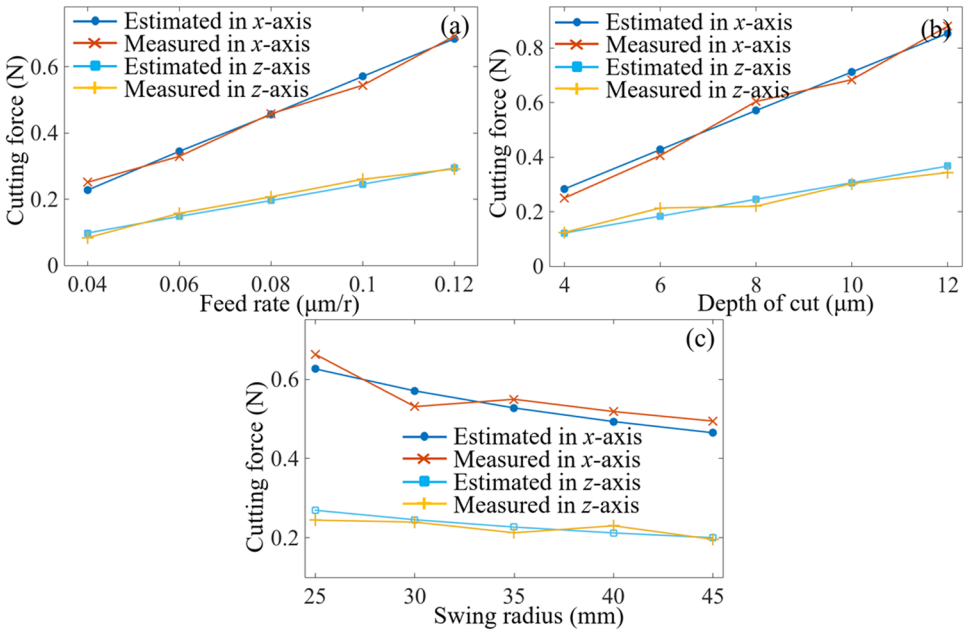

Fig. 12 A comparison of the estimated and measured cutting forces at different **a** feed rates, **b** depths of cut, and **c** swing radius

experimental results, validating the effectiveness of the proposed model as well as validating the necessary to consider the kinematics, tool geometry, and chip formation in force modeling. Besides, the accurate estimation of flow stress is the premise of analytical force modelling. The simulation results and observed chip micro-topographies verify that the proposed HSLM can well capture the flow stress variation from compressive to tensile with increasing chip thickness, owing to the consideration of size effect and material microstructure. When the UDCT is very small, the rubbing forces induced by material elastic recovery cannot be determined by the HSLM. In this study, the rubbing forces are determined by assuming its value to be proportional to the tool-chip interference volume, which has been validated by [4, 12].

5 Conclusions

An analytical cutting force model for ultra-precision fly grooving (UPFG) is proposed in this study with the full consideration of the kinematics, trans-scale variation of undeformed chip thickness (UDCT), material microstructure, and size effect. By dividing the workpiece into two layers, namely, surface and inner layers, a hybrid slip-line model (HSLM) is developed to calculate the flow stress in primary deformation zone. The normal cutting force and frictional cutting force are determined by analyzing the stress distribution and the frictional states in the secondary deformation zone using a tool-chip contact model. Besides, the rubbing force induced by elastic recovery is determined by assuming its value is proportional to the tool-workpiece interference

volume. Discrete and summation methods are employed for each discrete element of the chip to obtain the impulse cutting force. The free-vibration force generated by the temporary impact on dynameter is also determined by proposing a dynamic model, thereby to obtain the whole cutting force of UPFG. The proposed model is experimentally validated by UPFG of polycrystalline copper with different machining parameters, and the following conclusions can be drawn:

- The unique kinematics of UPFG leads to the axisymmetric chip morphology featuring ever-changing cross-sectional area with tool rotation. For each tool rotational cycle, the trans-scale variation of UDCT from nanoscale to microscale results in the periodic transformation of cutting mechanism from ploughing to shearing in UPFG. This also leads to the variation of chip micro-topography from relatively smooth surface to intensive lamella-like structures.
- The novelty of the proposed HSLM lies in its capability to determine the contribution of size effect and material microstructure, such as grain size, dislocation density, and crystal orientation, on the flow stress. By correlating the simulation results and the formed chip micro-topographies in UPFG, it is demonstrated that the proposed HSLM is able to capture the transformation of flow stress from tensile (shearing) to compressive (ploughing) with decreasing UDCT.
- The cutting force of UPFG is coupled by two main parts, namely, the impulse cutting force generated by the tool-workpiece interactions and the free-vibration force generated by the transient impact of the tool on dynameter. The estimated impulse cutting forces agree well with the corresponding experimental results with the estimation errors lower than 0.05 N, validating the effectiveness of the proposed model.
- According to the estimated and experimental results, it is learned that the maximum value of the impulse cutting force increases with the increase of feed rate and depth of cut. Nevertheless, the maximum cutting force decreases with the increase of the swing radius of the diamond tool. This is due to that much thinner chips are generated in UPFG with larger swing radius.

Funding This work is supported by the National Natural Science Foundation of China (NSFC Project No. 52005110, No. 51975128) and the European Commission/Research Grants Council Collaboration Scheme (Grant number E-PolyU502/17) and the Innovation and Technology Commission (ITF Project No. ITS/246/18FX).

Availability of data and material The datasets used or analyzed during the current study are available from the corresponding author on reasonable request.

Code availability Not applicable.

Declarations

Conflict of interest We declare no competing interests.

References

1. Zhang SJ, Zhou YP, Zhang HJ, Xiong ZW, To S (2019) Advances in ultra-precision machining of micro-structured functional surfaces and their typical applications. Int J Mach Tool Manu 142:16–41
2. Sun ZW, To S, Wang SJ, Du JJ (2020) Development of self-tuned diamond milling system for fabricating infrared micro-optics arrays with enhanced surface uniformity and machining efficiency. Opt Express 28:2221–2237
3. Zhang H, Zeng HH, Yan R, Wang W, Peng FY (2021) Analytical modeling of cutting forces considering material softening effect in laser-assisted milling of AerMet100 steel. Int J Adv Manuf Tech 113:247–260
4. Zhu ZW, To S, Zhu WL, Huang P, Zhou XQ (2019) Cutting forces in fast-/slow tool servo diamond turning of micro-structured surfaces. Int J Mach Tool Manu 136:62–75
5. Liu Y, Liu ZB, Wang XB, Huang T (2020) Experimental study on tool wear in ultrasonic vibration–assisted milling of C/SiC composites. Int J Adv Manuf Tech 107:425–436
6. Chen YL, Cai YD, Tohyama K, Shimizu Y, Ito S, Gao W (2017) Auto-tracking single point diamond cutting on non-planar brittle material substrates by a high-rigidity force controlled fast tool servo. Precis Eng 49:253–261
7. Sun ZW, To S, Yu KM (2018) An investigation in the ultra-precision fly cutting of freeform surfaces on brittle materials with high machining efficiency and low tool wear. Int J Adv Manuf Tech 101:1583–1593
8. Sun ZW, To S, Zhang SJ (2018) A novel ductile machining model of single-crystal silicon for freeform surfaces with large azimuthal height variation by ultra-precision fly cutting. Int J Mach Tool Manu 135:1–11
9. Ebrahimi R, Shafiei E (2012) Mathematical modeling of single peak dynamic recrystallization flow stress curves in metallic alloys. InTech, London
10 Zhang GQ, Ran JQ, To S, Wu XY, Huang P, Kuz'min MP (2020) Size effect on surface generation of multiphase alloys in ultra-precision fly cutting. J Manuf Process 60:23–36
11. Huang P, Lee WB (2016) Cutting force prediction for ultra-precision diamond turning by considering the effect of tool edge radius. Int J Mach Tool Manu 109:1–7
12. Sun ZW, To S, Wang SJ (2019) An analytical force model for ultra-precision diamond sculpturing of micro-grooves with textured surfaces. Int J Mech Sci 160:129–139
13. Fernando PKSC, Pei ZJ, Zhang M (2020) Mechanistic cutting force model for rotary ultrasonic machining of rocks. Int J Adv Manuf Tech 109:109–128
14. Zhu ZR, Wu JW, Yan R, Peng FY, Tang XW (2021) Cutting force prediction considering tool path curvature and torsion based on screw theory. Int J Adv Manuf Tech 114:1601–1621
15. Gap Y, Kim J, Ni M, Koc, (2007) Modeling of the size effects on the behavior of metals in microscale deformation processes. J Manuf Sci E 129:470–476
16. Ran JQ, Fu MW (2014) A hybrid model for analysis of ductile fracture in micro-scaled plastic deformation of multiphase alloys. Int J Plasticity 61:1–16

17. Chen N, Chen MJ, Wu CY, Pei XD, Qian J, Reynaerts D (2017) Research in minimum undeformed chip thickness and size effect in micro end-milling of potassium dihydrogen phosphate crystal. Int J Mech Sci 134:387–398
18. Kim YC, Gwak EJ, Ahn SM, Kang NR, Han HN, Jang JI, Kim JY (2018) Indentation size effect for spherical nanoindentation on nanoporous gold. Scripta Mater 143:10–14
19. Lai XM, Peng LF, Hu P, Lan SH, Ni J (2008) Material behavior modelling in micro/meso-scale forming process with considering size/scale effects. Comp Mater Sci 43:1003–1009
20. Fang N, Jawahir IS, Oxley PLB (2001) A universal slip-line model with non-unique solutions for machining with curled chip formation and a restricted contact tool. Int J Mech Sci 43:557–580
21. Ke QC, Xu DC, Xiong DP (2017) Cutting zone area and chip morphology in high-speed cutting of titanium alloy Ti-6Al-4V. J Mech Sci Technol 31:309–316
22. Ren H, Altintas Y (2000) Mechanics of machining with chamfered tools. J Manuf Sci E 122:650
23. Hu C, Z KJ, Weng J, Zhang XM (2019) Thermal-mechanical model for cutting with negative rake angle based on a modified slip-line field approach. Int J Mech Sci 164:105167
24. Peng LF, Lai XM, Lee HJ, Song JH, Ni J (2009) Analysis of micro/mesoscale sheet forming process with uniform size dependent material constitutive model. Mat Sci Eng A-Struct 526:93–99
25. Han JJ, Lin Y, Zheng W, Wang GC (2020) Experimental and numerical investigations on size effect of friction in meso-/micro-forming without lubricant. Int J Adv Manuf Tech 106:4869–4877
26. Ashby MF (1970) The deformation of plastically non-homogeneous materials. The Philosophical Magazine: A Journal of Theoretical Experimental and Applied Physics 21:399–424
27. Oxley PLB, Hastings WF (1977) Predicting the strain rate in the zone of intense shear in which the chip is formed in machining from the dynamic flow stress properties of the work material and the cutting conditions. Proceedings of the Royal Society of London A Mathematical and Physical Sciences 356:395–410
28. Wang ZF, Zhang JJ, Xu ZW, Zhang JG, Sun T (2020) Crystal anisotropy-dependent shear angle variation in orthogonal cutting of single crystalline copper. Precis Eng 63:41–48
29. Sakkaki M, Moghanlou FS, Vajdi M, Pishgar F, Shokouhimehr M, Asl MS (2019) The effect of thermal contact resistance on the temperature distribution in a WC made cutting tool. Ceram Int 45:22196–22202
30. Kuznetsov V, Shlyk YK, Vedernikova YA, Nekrasov RY, Kokorin IN (2020) Thermoelectric model of the cutting process. Russ Eng Res 40:518–521
31. Boothroyd G (1996) Temperatures in Orthogonal Metal Cutting. P I Mech Eng 177:789–810
32. Wang ZG, Rahman M, Wong YS, Li XP (2005) A hybrid cutting force model for high-speed milling of titanium alloys. Cirp Ann-Manuf Techn 54:71–74
33. Rahman MA, Rahman M, Kumar AS (2017) Modelling of flow stress by correlating the material grain size and chip thickness in ultra-precision machining. Int J Mach Tool Manu 123:57–75
34. Wang ZF, Zhang JJ, Xu ZW, Zhang JG, Ul Hassan H, Li G et al (2019) Crystal plasticity finite element modeling and simulation of diamond cutting of polycrystalline copper. J Manuf Process 38:187–195
35. Ran JQ, Fu MW, Chan WL (2013) The influence of size effect on the ductile fracture in micro-scaled plastic deformation. Int J Plasticity 41:65–81
36. Johnson GR (1983) A constitutive model and data for materials subjected to large strains, high strain rates, and high temperatures. Proc 7th Inf Sympo Ballistics 19:541–7
37. Demir E (2008) Taylor-based model for micro-machining of single crystal fcc materials including frictional effects—application to micro-milling process. Int J Mach Tool Manu 48:1592–1598
38. Clausen B, Lorentzen T, Leffers T (1998) Self-consistent modelling of the plastic deformation of fcc polycrystals and its implications for diffraction measurements of internal stresses. Acta Mater 46:3087–3098